

1     **New insights into the differences between the dual node approach**  
2     **and the common node approach for coupling surface-subsurface**  
3                     **flow**

4  
5     Rob de Rooij

6     Water Institute, University of Florida, 570 Weil Hall, PO Box 116601, Gainesville, FL-32611-  
7     6601, USA

8     r.derooij@ufl.edu

9

10    Corresponding author:

11    Rob de Rooij

12    Water Institute

13    University of Florida

14    570 Weil Hall

15    PO Box 116601

16    Gainesville

17    FL-32611-6601

18    USA

19    Telephone: 1-352-392-5893

20    Fax: 1-352-392-6855

21 **Key points**

22 Surface-subsurface flow coupling

23

24

25

26

27

28

29

30

31

32

33

34

35

36

37

38

39

40

41

42 **Abstract**

43 The common node approach and the dual node approach are two widely applied approaches to  
44 couple surface-subsurface flow. In this study both approaches are analyzed for cell-centered as  
45 well as vertex-centered finite difference schemes. It is shown that the dual node approach should  
46 be conceptualized and implemented as a one-sided first-order finite-difference to approximate the  
47 vertical subsurface hydraulic gradient at the land surface. This results in a consistent dual node  
48 approach in which the coupling length is related to grid topology. In this coupling approach the  
49 coupling length is not to be interpreted as a non-physical model parameter. Although, this  
50 particular coupling approach is technically not new, the differences between this consistent dual  
51 node approach and the common node approach have not been studied in detail. In fact, this  
52 coupling scheme is often believed to be similar to the common node approach. In this study it is  
53 illustrated that in comparison to the common node approach, the head continuity at the surface-  
54 subsurface interface is formulated more correctly in the consistent dual node approach. Numerical  
55 experiments indicate that the consistent dual node approach is less sensitive to the vertical  
56 discretization when simulating excess infiltration. It is also found that the consistent dual node  
57 approach can be advantageous in terms of numerical efficiency.

58

59

60

61

62

## 63 1 Introduction

64 There exists a variety of hydrogeological problems, such as the hydrologic response of hillslopes  
65 and river catchments, which requires an integrated analysis of surface and subsurface flows. This  
66 has led to the development of physically-based, distributed parameter models for simulating  
67 coupled surface-subsurface flows. Well-known examples of such models include MODHMS [  
68 *Panday and Huyakorn, 2004*], InHM [*Ebel et al., 2009*], HydroGeoSphere [*Therrien et al., 2010*],  
69 CATHY [*Camporese et al., 2010*], WASH123D [*Yeh et al., 2011*], ParFlow [*Kollet and Maxwell,*  
70 2006] and OpenGeoSys [*Kolditz and Shao, 2010*]. Typically, subsurface flow is governed by the  
71 Richards' equation whereas surface flow is either governed by the kinematic wave or the diffusive  
72 wave equation.

73 The coupling between subsurface and surface flow may be either based on the common  
74 node approach [*Kollet and Maxwell, 2006*] or on the dual node approach [*Ebel et al., 2009; Panday*  
75 *and Huyakorn, 2004; VanderKwaak, 1999*]. In the common node approach coupling is formulated  
76 by a continuity in head between surface and subsurface nodes. The dual node approach is based  
77 on formulating an exchange flux between the surface and subsurface nodes. Typically, the dual  
78 node approach is conceptualized as a hydraulic separation of the surface and the subsurface by an  
79 interface with a given thickness [*Liggett et al., 2012*]. The thickness of this interface defines a  
80 coupling length between the dual nodes to formulate the discrete exchange flux between the dual  
81 nodes.

82 It has been argued that the coupling length represents a non-physical model parameter,  
83 because there is often no evidence to support the existence of a distinct interface between the two  
84 flow domains [*Kollet and Maxwell, 2006*]. As such it appears that the common node approach is  
85 a more physically based coupling approach [*Kollet and Maxwell, 2006; Liggett et al., 2012*]. It has

86 also been found that accurate simulations based on the dual node approach typically require a very  
87 small coupling length [Ebel *et al.*, 2009; Liggett *et al.*, 2012; Liggett *et al.*, 2013]. Since it is known  
88 that the dual node approach mimics the common node in the limit as the coupling length goes to  
89 zero [Ebel *et al.*, 2009], it thus seems that the dual node approach is most accurate if it mimics the  
90 common node approach. Nonetheless, it has been argued that the dual node approach remains an  
91 attractive alternative coupling approach since it offers more flexibility than the common node  
92 approach. Namely, while it can mimic the common node approach, the dual node approach offers  
93 the possibility to simulate a less tight coupling of surface-subsurface flow which results in  
94 increased computational efficiency [Ebel *et al.*, 2009].

95         In this study a detailed analysis of both coupling approaches is provided for cell-centered  
96 as well as vertex-centered finite difference schemes. This analysis starts with the crucial  
97 observation that that the topmost subsurface nodal values as computed by the finite difference  
98 schemes represent the mean values within the topmost discrete control volumes. Numerical  
99 experiments to compare the coupling approaches are carried out with the model code DisCo [de  
100 Rooij *et al.*, 2013]. It is shown that the dual node approach should be interpreted and implemented  
101 as a one-sided finite difference approximation of the vertical hydraulic gradient at the land surface.  
102 This yields a consistent dual node scheme in which the coupling length is defined by the half the  
103 thickness of the topmost subsurface cells. The scheme of An and Yu [An and Yu, 2014] as well as  
104 the scheme of Kumar *et al.* [Kumar *et al.*, 2009] are essentially very similar to this consistent dual  
105 node scheme. In the work of Panday and Huyakorn [Panday and Huyakorn, 2004], one of the  
106 suggestions to define the coupling length is to use half the thickness of the topmost subsurface  
107 cells, which yields a consistent dual node scheme. While the idea that the coupling length can be  
108 based on the grid topology is not new [Panday and Huyakorn, 2004], the idea that it must be

109 related to grid topology to obtain a consistent approach is a significant new insight. Namely, since  
110 the coupling length in the consistent dual node approach is not to be interpreted as the thickness  
111 of a layer that separates the subsurface from the surface, the consistent dual node approach is not  
112 automatically less physically based than the common node. In fact, as explained in this study in  
113 comparison to the common node approach the implementation of a head continuity at the surface-  
114 subsurface interface is formulated more correctly in the consistent dual node approach.

115         The current consensus about how the dual node approach compares to the common node  
116 approach is based on alternative dual node approaches which as explained in this study are  
117 different from the consistent dual node approach. In this study the consistent dual node approach  
118 is compared in detail with the common node approach. It is shown that if the vertical discretization  
119 is sufficiently fine, then the common node approach and the consistent dual node approach are  
120 equally accurate. However, when simulating excess infiltration the consistent dual node approach  
121 is found to be less sensitive to the vertical discretization in comparison to the common node  
122 approach. This advantage in accuracy is related to the fact that head continuity is more correctly  
123 formulated in the consistent dual node approach. Moreover, it is also shown that the consistent  
124 dual node approach can be advantages in terms of numerical efficiency when simulating runoff  
125 due to both excess saturation as well as excess infiltration. The finding of this study show that the  
126 consistent dual node approach compares more positively with respect to the common node  
127 approach than other dual node approaches.

## 128 **2 Interpretation of nodal values**

129 As explained later on, a correct interpretation of nodal values is crucial for understanding the dual  
130 and common node approach for coupling surface-subsurface flow. Moreover, both coupling

131 approaches depend on the configuration of surface and topmost subsurface nodes near the land  
132 surface. This configuration depends on whether cell-centered or vertex-centered schemes are used.  
133 In this study both type of schemes will be covered, but for simplicity only finite difference schemes  
134 are considered.

135         In both cell-centered as vertex-centered schemes the flow variables such as the heads and  
136 the saturation are computed on nodes. In vertex-centered schemes these nodes coincide with the  
137 vertices of the mesh, whereas in cell-centered schemes the nodes coincide with the cell centers.  
138 When employing a finite difference scheme, nodal values correspond to the mean value within  
139 surrounding discrete control volumes. In cell-centered finite difference schemes these discrete  
140 volumes are defined by the primary grid cells. In vertex-centered finite difference schemes these  
141 discrete volumes are defined by the dual grid cells. Ideally, the mean values in the discrete control  
142 volumes are derived by applying the midpoint rule for numerical integration such that their  
143 approximation is second-order accurate. Therefore, the nodal values should ideally represent  
144 values at the centroid of the surrounding discrete control volume [Blazek, 2005; Moukalled *et al.*,  
145 2016]. In that regard, a cell-centered finite difference scheme is thus more accurate than a vertex-  
146 centered finite difference scheme. Namely, in cell-centered finite difference schemes the nodal  
147 values always correspond to the centroids of the cell whereas in vertex-centered finite difference  
148 schemes nodes and centroids (of the dual cells) do not coincide at model boundaries and in model  
149 regions where the primary grid is not uniform. It is well-known that this mismatch between nodes  
150 and centroids can lead to inaccuracies since the mean values within affected discrete volumes are  
151 not computed by a midpoint rule [Blazek, 2005; Moukalled *et al.*, 2016].

152         Typically, vertex-centered schemes for simulating coupled surface-subsurface flow are  
153 based on mass-lumped finite element schemes [Liggett *et al.*, 2012] and not on finite difference

154 schemes. However, with respect to coupling surface-subsurface flow there is actually no difference  
155 between a mass-lumped finite element scheme and a vertex-centered finite difference scheme.  
156 Similar as in vertex-centered finite difference schemes, the nodal values in mass-lumped finite  
157 element schemes define the mean values inside dual grid cells [Zienkiewicz *et al.*, 2005].  
158 Moreover, the coupling approaches establish one-to-one relations between surface and topmost  
159 subsurface nodes which do not depend on whether a finite difference or a finite element approach  
160 is being used.

### 161 **3 Common node approach**

162 The common node approach defines a head continuity between the topmost subsurface nodes and  
163 the surface nodes. This continuity requires that the topmost subsurface nodes and the surface nodes  
164 are co-located at the land surface such that there exists a continuity in the elevation head. This  
165 requirement is automatically full-filled in vertex-centered schemes. Figure 1a illustrates the  
166 configuration of common nodes in ParFlow, a cell-centered scheme [personal communication  
167 Maxwell, R. in relation to previous work of the author [De Rooij *et al.*, 2012]]. Figure 1c illustrates  
168 the configuration of common nodes for vertex-centered schemes. This configuration is similar to  
169 the configuration as used in HydroGeoSphere [Therrien *et al.*, 2010].

170         Considering that nodal values represent ideally the mean values within discrete control  
171 volumes as described in Section 2, it can be argued that the head continuity as implemented in the  
172 common node approach is not in agreement with the physical principle of head continuity at the  
173 land surface. Namely, the common node approach enforces a continuity between surface heads at  
174 the land surface and the mean subsurface heads within the topmost subsurface discrete control  
175 volumes which have a finite thickness. This is different from enforcing a continuity between



176 surface heads and subsurface heads within an infinitesimal thin subsurface layer directly below the  
177 land surface. As such the common node approach is only numerically correct if the topmost  
178 subsurface cells are very thin.

## 179 **4 Dual node approach**

### 180 **4.1 Basics**

181 Figure 1b and 1c illustrate the classical arrangement of surface and subsurface nodes in cell-  
182 centered and vertex-centered finite difference schemes, respectively. Commonly, the dual node  
183 approach is expressed in terms of an exchange flux  $q_e$  [ $\text{LT}^{-1}$ ] computed as [Liggett *et al.*, 2012;  
184 Panday and Huyakorn, 2004]:

$$185 \quad q_e = f_p \frac{K_z}{l} (h_s - h_{ss}) \quad (1)$$

186 where  $h_s$  and  $h_{ss}$  are the hydraulic heads [L] associated with the surface node and the topmost  
187 subsurface node, respectively,  $f_p$  [-] the fraction of the interface that is ponded and  $l$  the coupling  
188 length [L]. The ponded fraction of the interface is typically defined by a function that varies  
189 smoothly between zero at the land surface elevation and unity at the rill storage height which  
190 defines the minimum water depth for initiating lateral overland flow [Panday and Huyakorn,  
191 2004]. In equation (1) the term  $f_p K_z / l$  is commonly referred to as the first-order exchange  
192 parameter, where first-order means that the exchange flux depends linearly of the hydraulic head  
193 difference.

194 Typically, equation (1) is not derived as a numerical approximation of basic flow equations  
195 that govern the exchange flux, but is merely presented a numerical technique to couple two  
196 different flow domains [Ebel *et al.*, 2009; Liggett *et al.*, 2012]. Subsequently, the dual node

197 approach is conceptualized by interpreting equation (1) as an expression that describes  
 198 groundwater flow across a distinct interface separating the two flow domains [Ebel *et al.*, 2009;  
 199 Liggett *et al.*, 2012; Liggett *et al.*, 2013].

## 200 4.2 Consistent dual node approach

201 In the following, it is illustrated that the dual node approach can and should be derived from basic  
 202 equations that describe infiltration into a porous medium. Using Darcy's Law, the infiltration rate  
 203 at the ponded land surface  $q_{s \rightarrow ss}$  [ $LT^{-1}$ ] can be written as a function of the vertical subsurface  
 204 hydraulic gradient at the land surface:

$$205 \quad q_{s \rightarrow ss} = \left( k_r K_z \frac{\partial h}{\partial z} \right) \Big|_{z=z_s} = K_z \frac{\partial h}{\partial z} \Big|_{z=z_s} \quad (2)$$

206 where  $h$  the hydraulic head [L],  $z$  the elevation head [L],  $k_r$  the relative hydraulic conductivity [-]  
 207  $K_z$  the saturated vertical hydraulic conductivity [ $LT^{-1}$ ] and  $z_s$  the elevation head at the land surface.  
 208 The relative hydraulic conductivity is unity because equation (2) applies to the ponded land surface  
 209 which implies fully saturated conditions at the land surface (i.e. ponding means  $p_s > 0$ , where  $p_s$  is  
 210 the pressure head at the surface). Similarly, the infiltrability [ $LT^{-1}$ ], defined as the infiltration rate  
 211 under the condition of atmospheric pressure [Hillel, 1982], can be written as:

$$212 \quad I = \left( k_r K_z \frac{\partial h}{\partial z} \right) \Big|_{z=z_s, p_s=0} = K_z \frac{\partial h}{\partial z} \Big|_{z=z_s} \quad (3)$$

213 The relative hydraulic conductivity is again unity because the saturation equals unity under  
 214 atmospheric conditions ( $p_s = 0$ ). The infiltration rate at non-ponded land surface  $q_{atm \rightarrow ss}$  [ $LT^{-1}$ ] can  
 215 be expressed as:

$$216 \quad q_{atm \rightarrow ss} = \min \left( \max (I, 0), q_R \right) \quad (4)$$

217 where  $q_R$  is the effective rainfall rate (i.e. the infiltration rate is limited by either the infiltrability  
 218 or the available effective rainfall rate). The total exchange flux across the surface-subsurface  
 219 interface can now be written as:

$$220 \quad q_e = f_p q_{s \rightarrow ss} + (1 - f_p) q_{atm \rightarrow ss} \quad (5)$$

221 To approximate the vertical subsurface hydraulic gradient in equations (2) and (3), it is  
 222 crucial to recognize that according to the principle of head continuity at the land surface, the  
 223 surface hydraulic head at a surface node must also represent the subsurface head at the land surface  
 224 at that location. Moreover, since the subsurface hydraulic heads at the topmost subsurface nodes  
 225 are ideally associated with the centroids of the topmost subsurface discrete control volumes, these  
 226 head values do not represent values at the land surface but at some depth below the land surface.  
 227 Because the subsurface hydraulic heads at the dual nodes can be and should be associated with a  
 228 different elevation, the vertical subsurface head gradient between the dual nodes can be  
 229 approximated by a standard finite difference approximation. If this approximation is being used to  
 230 approximate the gradient at the land surface in equations (2) and (3), then this approximation is by  
 231 definition a one-sided first-order finite difference. By defining the coupling length by  $l = \Delta z_{dn}$   
 232 where  $\Delta z_{dn}$  is the difference in the mean elevation head associated with the dual nodes, the  
 233 infiltration rate and infiltrability can thus be computed with the following one-sided finite  
 234 difference approximation:

$$235 \quad K_z \left. \frac{\partial h}{\partial z} \right|_{z=z_s} \approx \frac{K_z}{l} (h_s - h_{ss}) \quad (6)$$

236 The above definition of the coupling length  $l = \Delta z_{dn}$  ensures a proper approximation of the vertical  
 237 gradient in elevation head at the land surface:

238 
$$\left. \frac{\partial z}{\partial z} \right|_{z=z_s} = \frac{\Delta z_{dn}}{l} = 1 \quad (7)$$

239 The above derivation of the consistent dual node approach from basic flow equations has  
240 implications for how the dual node approach is conceptualized and how it should be implemented.  
241 The idea that the coupling length must be directly related to the spatial discretization is an  
242 important new insight. Namely, as the coupling length is related to grid topology, it does not  
243 represent a non-physical parameter associated with a distinct interface separating the two domains.  
244 It is also crucial to observe the difference between the consistent dual node approach and the  
245 common node approach regarding how the head continuity at the surface-subsurface interface is  
246 formulated. As explained in Section 2, the formulation in the common node approach is only  
247 correct if the topmost subsurface discrete volumes are very thin. In comparison, the formulation  
248 in the dual node approach is correct irrespective of the vertical discretization. Namely, irrespective  
249 of the vertical discretization the surface hydraulic heads equal the subsurface heads at the interface.

250 Since nodal values in cell-centered scheme are located at the centroids of the cells, the  
251 coupling length is simply given by  $l = z_s - z_{ss}$  where  $z_s$  and  $z_{ss}$  are the elevation heads [L] associated  
252 with the surface node and the topmost subsurface node, respectively. This value for the coupling  
253 length in cell-centered schemes has also been suggested by Panday and Huyakorn [*Panday and*  
254 *Huyakorn, 2004*]. However, in their work, the particular advantage of choosing this value (i.e.  
255 maintaining a unit gradient in elevation head) is not recognized. The coupling schemes as used by  
256 An and Yu [*An and Yu, 2014*] and Kumar et al. [*Kumar et al., 2009*] are also in essence consistent  
257 dual node schemes. However, these schemes are not recognized as a dual node scheme. Instead,  
258 An and Yu [*An and Yu, 2014*] argue that their scheme is similar to the common node approach of  
259 Kollet and Maxwell [*Kollet and Maxwell, 2006*]. Kumar et al. [*Kumar et al., 2009*] argue that their

260 scheme is similar to the dual node approach if the coupling length goes to zero which implies that  
261 their scheme would be similar to the common node approach. However, contrary to the common  
262 node approach the schemes of An and Yu [*An and Yu, 2014*] and Kumar et al. [*Kumar et al., 2009*]  
263 compute exchange fluxes between surface and topmost subsurface nodes and therefore these  
264 schemes are technically dual node schemes. As explained in this study, it is crucial to observe that  
265 the schemes of An and Yu [*An and Yu, 2014*] and Kumar et al. [*Kumar et al., 2009*] are actually  
266 quite different from the common node approach. As already mentioned, the consistent dual node  
267 scheme differs from the common node approach with respect to how the head continuity is  
268 formulated at the surface-subsurface interface. As discussed later on, this difference has crucial  
269 consequences in terms of accuracy as well as numerical efficiency.

270         In vertex-centered schemes the commonly used nodal configuration near the surface is such  
271 that  $z_s = z_{ss}$ . However, even though the topmost subsurface node is located at the land surface in a  
272 vertex-centered scheme, the elevation head at this node should ideally correspond to the mean  
273 elevation head within the topmost subsurface discrete volume. This suggests that the topmost  
274 subsurface node should be moved to the centroid of the topmost subsurface discrete volume.  
275 Although this is a possible solution, the drawback of this solution is that the subsurface model  
276 ceases to be a purely vertex-centered scheme. Moreover, such an operation cannot be performed  
277 in finite element schemes since the nodal positions define the geometry of the elements. Therefore,  
278 an alternative solution is proposed. Namely, in vertex-centered schemes the elevation of the  
279 surface nodes are changed according to  $z_s = z_{ss} + l$  where  $l$  is equals half the thickness of the  
280 topmost subsurface dual cell. The resulting nodal configuration is illustrated in Figure 1d. When  
281 applying this solution, all the topmost subsurface cells must have the same thickness, such that the  
282 topography is increased with the same value everywhere. In essence, the motivation behind this

283 solution is that a more accurate approximation the hydraulic gradient (i.e. enforcing a unit gradient  
 284 in elevation head) is more important than the actual elevation of the land surface. Similar to the  
 285 nodal configuration in ParFlow, the resulting nodal configuration may not seem ideal. Namely, the  
 286 surface elevation does not coincide with the top of the subsurface grid. Nonetheless, as illustrated  
 287 later on, simulation results obtained with the resulting scheme are reasonable.

288 To illustrate that the presented dual node approach exhibits consistent behaviour, the  
 289 necessary conditions for ponding due to excess infiltration and exfiltration are considered. In  
 290 general ponding starts when  $q_R > I$  [Hillel, 1982]. Observing that equation (6) defines the computed  
 291 infiltrability when  $p_s = 0$  and that the gradient in elevation head between the dual nodes is unity,  
 292 the infiltrability can be expressed by  $I = K_z (1 - p_{ss}/l)$ . Therefore,  $q_R > I$  implies that:

$$293 \quad p_{ss} > l \left( 1 - \frac{q_R}{K_z} \right) \quad (8)$$

294 Ponding due to excess infiltration occurs if  $q_R/K_z > 1$  and implies that saturation in the subsurface  
 295 starts from the top down [Hillel, 1982]. Using  $q_R/K_z > 1$  it follows from equation (8) that  $p_{ss}$  is  
 296 still negative at the moment of ponding. This is reasonable, because the pressure head value at the  
 297 topmost subsurface node represents a value at a certain depth below the land surface. Top-down  
 298 saturation implies that saturation at the topmost subsurface node occurs after ponding and thus a  
 299 negative pressure head value at this node at the moment that ponding starts. It is noted that if the  
 300 ratio  $q_R/K_z$  is greater than but close to unity or if the coupling length is very small, then this  
 301 condition becomes  $p_{ss} \approx 0$ . Once ponding starts the total flux rate between the dual nodes equals  
 302  $K_z ((p_s - p_{ss})/l + 1)$ . Top-down saturation requires that this flux exceeds the vertical hydraulic  
 303 conductivity. Reaching saturation at the topmost node ( $p_{ss} = 0$ ) therefore requires  $p_s \geq 0$ . Thus,

304 while  $p_{ss}$  is still negative at the moment that ponding starts, saturation at the topmost subsurface  
305 node will occur some time after ponding started. Ponding due to excess saturation occurs if  
306  $q_R/K_z < 1$  and implies that saturation in the subsurface starts from the bottom up [Hillel, 1982]. It  
307 follows from equation (8) that ponding due to excess saturation occurs while  $p_{ss} > 0$ . Thus ponding  
308 starts after reaching fully saturated conditions at the topmost subsurface node, which is again  
309 reasonable. It is noted that if the ratio  $q_R/K_z$  is smaller than but close to unity or if the coupling  
310 length is very small, then ponding occurs when  $p_{ss} \approx 0$ .

### 311 **4.3 Comparison to alternative coupling approaches**

312 To illustrate that it is crucial to account for the meaning of the values at the topmost subsurface  
313 nodes, it is instructive to consider what happens if these values are not taken as the mean values  
314 within discrete control volumes. As a first example, consider vertex-centered schemes where the  
315 dual nodes are defined such that  $z_{ss} = z_s$  as illustrated in Figure 1c. This is inconsistent because it  
316 defines a zero gradient in elevation head between the dual nodes. Since the vertical gradient in  
317 elevation head between the dual nodes is zero the total flux rate after ponding now equals  
318  $K_z(p_s - p_{ss})/l$ . Top-down saturation requires that this flux exceeds the vertical hydraulic  
319 conductivity. Thus, reaching saturation at the topmost subsurface node ( $p_{ss} = 0$ ) requires  $p_s > l$ .  
320 Therefore, top-down saturation will not occur if runoff occurs and if the surface water depths  
321 remains smaller than the chosen coupling length. Indeed, it has been pointed out in other studies  
322 that the coupling length should be smaller than the rill storage height [Delfs et al., 2009; Liggett et  
323 al., 2012]. The zero vertical gradient in elevation head between the dual nodal also means that the  
324 ponding occurs when  $p_{ss} > -lq_R/K_z$ . This implies that ponding due to excess saturation occurs

325 while the topmost subsurface node is not yet saturated. This dual node approach has been compared  
326 to the common node approach in vertex-centered schemes [Liggett *et al.*, 2012].

327 A second example is the dual node approach for cell-centered schemes as implemented in  
328 MODHMS which uses an adapted pressure-saturation relationship for the topmost subsurface  
329 nodes such that the topmost subsurface node only becomes fully saturated if hydraulic head at the  
330 node rises above the land surface [Liggett *et al.*, 2013]. Since the topmost subsurface heads are  
331 associated with the cell centroid, this dual node scheme defines a unit gradient in elevation head  
332 at the land surface. However, the saturation value at the topmost node is associated with a location  
333 at the land surface and not with the centroid of a discrete control volume. This has undesirable  
334 consequences. Namely, saturating the topmost subsurface node ( $p_{ss} = l$ ) due to excess infiltration  
335 requires that  $p_s > l$ . Indeed, when simulating excess infiltration with MODHMS, a very small  
336 coupling length is needed to simulate top-down saturation due to excess infiltration. [Gaukroger  
337 and Werner, 2011; Liggett *et al.*, 2013]. It can also be shown that ponding due to excess saturation  
338 occurs while  $p_{ss} > 0$ . But, because of the adapted pressure-saturation relationship this means that  
339 ponding starts while the topmost subsurface node is not yet saturated. This dual node approach has  
340 been compared to the common node approach in cell-centered schemes [Liggett *et al.*, 2013].

341 The two comparison studies of Liggett *et al.* [Liggett *et al.*, 2012; Liggett *et al.*, 2013]  
342 indicate that the dual node approach is typically only competitive with the common node approach  
343 in terms of accuracy once the coupling length is very small. However, the requirement for a very  
344 small coupling length, is a logical consequence if the topmost subsurface nodal values are not  
345 taken as the mean values within discrete volumes. In essence, by choosing a very small coupling  
346 length this inconsistency is minimized. This contrasts with the consistent dual approach in which



347 decreasing the coupling length for a given vertical discretization will result in more inaccurate  
348 simulation results as this would be numerically incorrect.

349 CATHY [Camporese *et al.*, 2010] as well as the model of Morita and Yen [Morita and  
350 Yen, 2002] are examples of models which are neither based on the common node approach, nor a  
351 dual node approach. Both these models are conjunctive models in which the surface and subsurface  
352 flow are computed separately in a sequential fashion and in which coupling is established by  
353 matching the flow conditions along the surface-subsurface interface. A complete discussion is  
354 outside the scope of this paper, but it is worthwhile to mention that these models share some crucial  
355 characteristics with the consistent dual node approach. Although the two models are different, both  
356 models switch between appropriate boundary conditions along the surface-subsurface interface,  
357 such that infiltration fluxes are limited to the infiltrability. In both models the infiltration fluxes  
358 are computed while accounting for the unit vertical gradient in elevation head near the surface-  
359 subsurface interface. In addition, in both models ponding occurs when the infiltrability is  
360 exceeded.

## 361 **5 Numerical experiments**

### 362 **5.1 Numerical model**

363 To compare the consistent dual node approach with respect to the common node approach in terms  
364 of accuracy and computational efficiency numerical experiments are presented. These experiments  
365 are carried out with the model code DisCo. This model code can simulate coupled surface-  
366 subsurface flow with the dual node approach using a fully implicit or monolithic scheme [de Rooij  
367 *et al.*, 2013]. Subsurface flow is governed by the Richards' equation while surface flow is governed  
368 by the diffusive wave equation.

369 Starting from a dual node scheme, the implementation of a common node scheme is  
370 relatively straightforward. If the surface nodes are numbered last, a permutation vector can be  
371 constructed which gives the corresponding topmost subsurface node for each surface node. Then,  
372 the node numbering as used in the original dual node scheme can still be used to compute the  
373 surface and subsurface flow terms. Subsequently, using the permutation vector the surface and  
374 subsurface flow terms associated with a common node can be combined into the same row of the  
375 global matrix system. In addition, when using the common node approach, there is no need to  
376 evaluate exchange flow terms between the two flow domains. It is noted that the surface flow and  
377 subsurface flow computations are exactly the same irrespective of the coupling approach. As such  
378 the model permits to compare the two approaches in terms of accuracy as well as numerical  
379 efficiency.

380 An adaptive error-controlled predictor-corrector one-step Newton scheme [*Diersch and*  
381 *Perrochet, 1999*] is used in which a single user-specified parameter controls the convergence as  
382 well the time stepping regime. Although, this scheme may not be necessary the most efficient  
383 scheme, it ensures that time discretization error is the same irrespective of the applied coupling  
384 approach. For brevity further details about the model are not discussed here and can be found  
385 elsewhere [*de Rooij et al., 2013*].

## 386 **5.2 Hillslope scenarios**

387 The model code is applied to a set of three hillslope scenarios. Table 1 lists the abbreviations used  
388 in the figures to distinguish between the coupling approaches, and to distinguish between cell-  
389 centered and vertex-centered schemes. Each scenarios is solved using different but uniform  
390 vertical discretizations and  $\Delta z$  specifies the discretization of the primary grid. The first two  
391 simulation scenarios consider hillslope problems as designed by Sulis et al. [*Sulis et al., 2010*].

392 For the purpose of this study, a third scenario is considered in which the initial and boundary  
393 conditions are different to create a flooding wave across an unsaturated hillslope. The problems  
394 consist of a land surface with a slope of 0.05 which is underlain by a porous medium. The domain  
395 is 400 m long and 80 m wide. The subsurface is 5 m thick. In the direction of the length and in the  
396 direction of the width the discretization is 80 m. Different vertical discretizations are considered.  
397 The van Genuchten parameters are given by  $s_r = 0.2$ ,  $s_s = 1.0$ ,  $\alpha = 1 \text{ m}^{-1}$  and  $n = 2$ . The porosity is  
398 0.4 and the specific storage is  $10^{-4} \text{ m}^{-1}$ . The Manning's roughness coefficients are given by  $3.3 \times$   
399  $10^{-4} \text{ m}^{-1/3} \text{ min}$ . The surface flow domain has a zero-gradient outflow condition. For the first two  
400 simulation scenarios the domain is recharged with an effective rainfall rate of  $3.3 \times 10^{-4} \text{ m/min}$  for  
401 a duration of 200 minutes and the initial water table depth is at a depth of 1.0 m below the land  
402 surface.

403 The first scenario considers excess saturation, the saturated conductivity equals  $6.94 \times 10^4$   
404  $\text{ m/min}$ . Figure 2 and 3 illustrates the simulated runoff and the number of Newton steps,  
405 respectively. Figure 4 and 5 illustrate the subsurface pressure heads at the topmost subsurface  
406 nodes and the water depths on the surface nodes. For the second scenario which considers excess  
407 infiltration the saturated hydraulic conductivity equals  $6.94 \times 10^{-7} \text{ m/min}$ . Figure 6 and 7 show the  
408 simulated runoff and the number of Newton steps, respectively. Figure 8 and 9 illustrate the  
409 subsurface pressure heads at the topmost subsurface nodes and the water depths on the surface  
410 nodes for the finest and the coarsest vertical discretization, respectively. In the third scenario a  
411 surface water flood wave crossing the hillslope in the downhill direction is simulated by applying  
412 a Neumann boundary condition of  $1.0 \text{ m}^3/\text{s}$  for a duration of 200 minutes to the surface nodes with  
413 the highest elevation. The initial water table is located at a depth of 1.5 m. The vertical saturated  
414 hydraulic conductivity equals  $6.94 \times 10^{-6} \text{ m/min}$ . Figure 10 illustrates the differences in simulated

415 runoff and Figure 11 illustrates the number of Newton steps of the model runs. Figure 12 and 13  
416 illustrate the subsurface pressure heads at the topmost subsurface nodes and the water depths on  
417 the surface nodes for the finest and the coarsest vertical discretization, respectively.

## 418 **6 Discussion**

### 419 **6.1 Accuracy**

420 As discussed by Ebel et al. [Ebel et al., 2009] and confirmed by others [Liggett et al., 2012] the  
421 dual node approach mimics the common node approach if the coupling length becomes sufficiently  
422 small. When comparing the consistent dual node approach and the common node approach a very  
423 similar observation applies. If the topmost subsurface cells are very thin, then the coupling length  
424 in the consistent dual node approach is very small. Also, if the topmost subsurface cells are  
425 sufficiently thin then the formulation of head continuity at the surface-subsurface interface in the  
426 common node approach is correct. Thus, the common node approach will mimic the consistent  
427 dual node approach. Indeed, the simulations results indicate that a relatively fine vertical  
428 discretization yields similar results for the common node approach as well as for the consistent  
429 dual node approach (Figure 2a, 4a, 6a, 8a, 10a and 12a).

430 A relatively fine uniform vertical discretisation also enables to simulate sharp saturation  
431 fronts with the Richards' equation [Pan and Wierenga, 1995; Ross, 1990]. As such the simulation  
432 results based on the finest vertical discretization can be taken as reference solutions that enables  
433 comparisons of the coupling approaches when a coarser vertical discretization is used.

#### 434 **6.1.1 Excess saturation**

435 The simulation results of runoff due to excess saturation as obtained by the common node approach  
436 and the consistent dual node approach as depicted in Figure 2 illustrate that simulating excess

437 saturation runoff is not significantly affected by the vertical discretization. This is because the time  
438 needed to reach fully saturated conditions in the subsurface is a simple function of the flow  
439 boundary conditions and the initial water content. It is thus expected that the vertical discretization  
440 does not significantly affect the simulation of excess saturation. Although the vertical  
441 discretization may affect the computed initial water content, this effect is usually negligible. It has  
442 been found in other studies that the vertical discretization has little effect on simulated runoff due  
443 to excess saturation [Kollet and Maxwell, 2006; Sulis et al., 2010].

#### 444 **6.1.2 Excess infiltration**

445 When simulating excess infiltration the common node approach requires fully saturated conditions  
446 at the topmost subsurface node for ponding to occur. However, top-down saturation associated  
447 with excess infiltration implies that reaching fully saturated conditions in the topmost subsurface  
448 discrete volumes should requires more time than reaching fully saturated conditions at the land  
449 surface, especially if the vertical discretization is relatively coarse. It is thus expected that the  
450 common node approach delays runoff and that this delay increases for a coarser vertical  
451 discretization. In addition, if the saturation fronts are less sharp due to a relatively coarse vertical  
452 discretization, it takes more time to reach saturated conditions at the common node. This will  
453 further delay runoff. Indeed, the simulation results indicate clearly that runoff is delayed when  
454 using the common node approach, particularly if the vertical discretization is relatively coarse  
455 (Figure 6, 9a, 10 and 13a). It has also been found in other studies that the common node approach  
456 delays runoff due to excess infiltration if the vertical discretization is relatively coarse [Sulis et al.,  
457 2010].

458 As explained in Section 4.2, when using the consistent dual node approach, ponding due  
459 to excess infiltration occurs before reaching fully saturated conditions at the topmost subsurface

460 node. More specifically, ponding occurs when the infiltrability is exceeded. Compared to the  
461 condition for ponding in the common node approach this is arguably more correct. Namely, if  
462 saturation occurs from the top-down then the saturation at a certain depth occurs later than  
463 saturation at the land surface. Indeed, simulation results indicate that when simulating excess  
464 infiltration the consistent dual node approach is less sensitive to the vertical discretization in  
465 comparison to the common node approach. This is clearly indicated in Figure 6b-d, 9a, 10b-d and  
466 13a. To further explain this difference in accuracy, it is emphasized that the spatial resolution only  
467 affects the accuracy of the flow computations when using the consistent dual node approach and  
468 that the formulation of head continuity at the interface remains correct. In contrast, when using the  
469 common node approach, if the spatial resolution is too coarse then this does not only affect the  
470 accuracy of the flow computations but in addition the formulation of head continuity becomes  
471 incorrect. It must be emphasized, however, that regardless of the applied coupling approach, the  
472 vertical discretization must be relatively fine. As indicated by Figure 6b-d, 9a, 10b-d and 13a the  
473 difference between the simulated results and the reference solution increase for a coarser  
474 discretization. Eventually such differences will lead to unreasonable results regardless of the  
475 coupling approach.

476         It is interesting to note that An and Yu [*An and Yu, 2014*] also found that their model was  
477 less sensitive to the vertical discretization in comparison to ParFlow when simulating runoff due  
478 to excess infiltration. Whereas An and Yu [*An and Yu, 2014*] hypothesized that this difference in  
479 performance was related to using irregular grids instead of orthogonal grids as in ParFlow, it is  
480 argued here that this difference can be explained by the fact that both models use a different  
481 coupling approach.

482           Although the consistent dual node approach is less sensitive to the vertical discretization  
483 in comparison to the common node approach, it is useful to explain in detail how the vertical  
484 discretization affects the accuracy of the consistent dual node approach to the vertical  
485 discretization. A relatively coarse vertical discretization may result in an underestimation of the  
486 vertical pressure gradient at the land surface. This is because in a soil close to hydrostatic  
487 conditions the pressure heads increase with depth. Therefore, the infiltrability during the early  
488 stages of infiltration may be underestimated. If the applied flux rate is sufficiently large such that  
489 the underestimated infiltrability is exceeded, then runoff during the early stages will be  
490 overestimated. Figure 6d illustrates that the runoff as simulated with the cell-centered scheme, a  
491 relatively coarse vertical discretization and a consistent dual node approach is indeed  
492 overestimated at early times. During the later stages of infiltration the pressure head at the topmost  
493 subsurface node will be underestimated due to the combined effect of an underestimated  
494 infiltration rate and the overly diffused saturation fronts. This results in an overestimation of the  
495 infiltration rate in the later stages. Thus at some time after ponding has started, it is expected that  
496 the amount of runoff is underestimated.

497           If the underestimated infiltrability is not exceeded, then the overly diffused saturation fronts  
498 resulting from a relatively coarse vertical discretization will eventually lead to an underestimation  
499 of pressure head at the topmost subsurface node and as such the infiltrability may be overestimated  
500 at later times. Consequently, when using the consistent dual node approach runoff due to excess  
501 infiltration may be delayed. However, the delay in runoff as simulated by the consistent dual node  
502 approach will only equal the delay in runoff as simulated by the common node approach in the  
503 limit when  $q_R/K_z$  goes to unity. Namely, as explained in Section 4.2 if  $q_R/K_z$  goes to unity, then the  
504 consistent dual node approach behaves similar as a common node approach. However, in general,

505 if the consistent dual node approach delays runoff, this delay will be smaller than the delay in  
506 runoff as simulated by the common node approach.

507 Comparing Figure 12a and 13a it can be observed that if the vertical discretization is  
508 relatively coarse then a common node can act as an artificial barrier for a surface water wave  
509 advancing across an initially unsaturated subsurface domain. Namely, as the wave travels  
510 downstream the wave can only advance to the next common node once it is fully saturated. The  
511 effect of this artificial barrier is that the front of the surface water wave is steepened. In contrast,  
512 the consistent dual approach simulates a wave that becomes less steep as it advances downstream  
513 for relatively fine as well as relatively coarse vertical discretizations as depicted in Figure 13a.

514 As illustrated in Figure 6b-d, and 10b-d, if the coupling approach and the vertical  
515 discretization are identical, then the vertex-centered schemes are closer to the reference solution  
516 with respect to the cell-centered schemes. This difference results solely from the fact the primary  
517 mesh is the same for both schemes. As such the vertical extent of the topmost subsurface volumes  
518 is twice as small when using the vertex-centered scheme. This difference in vertical grid resolution  
519 near the land surface explains the differences between the schemes.

## 520 **6.2 Computational efficiency**

521 The computational efficiency of the schemes is measured in terms of the number of Newton steps.  
522 The number of Newton steps equals the number of times that the linearized system of equations is  
523 solved and this number depends on the time step sizes as well as the number of failed Newton  
524 steps. It is emphasized that the measured efficiency depends crucially on the applied model code.  
525 Nonetheless, as shown in the following, the measured differences in efficiencies can be explained  
526 in terms of abrupt changes in how fast pressure heads near the surface-subsurface interface are



527 evolving with time. Regardless of the type of scheme used to solve the non-linear flow equations,  
528 such abrupt changes are difficult to solve.

529         Once ponding occurs a surface-subsurface flow model will encounter significant numerical  
530 difficulties as surface flow terms are activated. In essence, the activation of these terms represents  
531 a discontinuity in flow behaviour which is challenging to resolve [*Osei-Kuffuor et al.*, 2014].  
532 Indeed, the Newton steps as depicted in Figure 3 and 7 indicate that simulations encounter  
533 difficulties at the moment of ponding. These figures also indicate that the consistent dual node  
534 approach can be more efficient in comparison to the common node approach.

### 535         **6.2.1 Excess saturation**

536 Just before the moment of ponding due to excess saturation, the rate of change in pressure heads  
537 at the topmost subsurface nodes is relatively high for both coupling approaches. This high rate is  
538 related to the shape of the water retention curve. Typically, the derivative of the saturation with  
539 respect to the pressure head goes to zero when approaching fully saturated conditions. Once  
540 ponding starts, the surface flow terms are activated and therefore the rate of changes in pressure  
541 heads at the topmost subsurface nodes decreases drastically. Both approaches must handle this  
542 drastic change. However, from Figure 4b and 5b it can be observed that the rate of change  
543 decreases more abruptly when using the common node approach.

544         When using the common node approach the vertical hydraulic gradients in the subsurface  
545 are close to zero at the moment of ponding, since additional water volumes can only be  
546 accommodated by means of specific storage. This implies that the infiltration rate drops  
547 instantaneously at the moment of ponding. In contrast, in the dual node approach ponding starts  
548 when the infiltrability is exceeded. Thus at the moment of ponding, the infiltration rate is higher  
549 in comparison to the common node approach. After ponding this infiltration rate will decrease

550 quickly as the hydraulic heads at the dual nodes equilibrate. This difference in the infiltration rate  
551 at the moment of ponding explains why the topmost subsurface hydraulic heads change more  
552 smoothly when using the dual node approach. If the vertical discretization is coarser, then the  
553 infiltration rate at the moment of ponding as computed with the consistent dual node approach is  
554 even higher and this results in a lower initial rate initial rate of change in water depth as depicted  
555 in Figure 5a.

556         The more abrupt changes in pressure heads at the common node in comparison to the  
557 changes in pressure heads at the dual nodes mean that solving the activation of ponding with the  
558 common node approach is more difficult. It is noted that the differences in the infiltration rates  
559 between the two coupling approaches only occur at the moment of ponding and directly thereafter  
560 when water depths are relatively small. Namely, quickly after ponding, the hydraulic heads at the  
561 dual nodes will equilibrate and after that the two coupling approaches will behave similar. This  
562 explains why these differences in infiltration rates do not significantly affect the accuracy of  
563 simulated runoff.

## 564         **6.2.2 Excess infiltration**

565 Figure 8, 9, 12 and 13 illustrate the evolution of pressure heads at dual nodes and common nodes  
566 when simulating excess infiltration. When applying the consistent dual approach, the net flux into  
567 a topmost subsurface cell will decrease once ponding occurs, because the applied flux rate will be  
568 partitioned between dual nodes (i.e. between the surface flow and subsurface flow domain). This  
569 occurs while the topmost subsurface node is not yet fully saturated. After ponding the infiltration  
570 rate decreases such that if the topmost subsurface node reaches fully saturated conditions the net  
571 flux into the topmost subsurface node is relatively small. In contrast, partitioning of the applied  
572 flux rate on a common node between the surface flow and subsurface domain starts when the

573 common node reaches fully saturated conditions at this node. This means that just before ponding  
574 the rate of change in pressure head is relatively high as the common node is driven towards fully  
575 saturated conditions while the infiltration rate is relatively high. This means that similar to the  
576 excess saturation scenario the rate of change in pressure head at the common node is high just  
577 before ponding. At the moment of ponding, this rate must drop abruptly as surface flow terms are  
578 activated. This abrupt change explains why the common node approach is less efficient.

579         Figures 7 and 11 also indicate that a coarser vertical discretization only provides a  
580 significant gain in efficiency in terms of Newton steps when using the consistent dual node  
581 approach. When using the common node approach, a coarser discretization does not change the  
582 fact that the topmost subsurface node must reach fully saturated conditions for ponding to occur  
583 and that the infiltration rate is relatively high just before ponding. When using the consistent dual  
584 node approach, a coarser vertical discretization means that the saturation fronts are more diffused  
585 such that the flow problem becomes easier to solve.

586         Figure 8a and 9a illustrate that for the second simulation scenario, ponding occurs almost  
587 simultaneously at all the surface nodes. Figure 12a and 13a show that this is different for the third  
588 scenario where ponding occurs at different times as the flooding wave travels downstream. When  
589 Figure 11a is compared with Figure 12a and when Figure 11d is compared with Figure 13a, it is  
590 clear that the common node approach encounters difficulties around each time ponding starts at a  
591 surface node. Figure 11 shows that these difficulties are encountered for all discretizations. In  
592 contrast the consistent dual node approach has much less difficulties solving these difficulties. As  
593 discussed in Section 6.1.2. the common node approach may result in steepening the advancing  
594 wave. This implies that water depths will be changing more quickly. This presents an additional  
595 difficulty for solving this flow problem with the common node approach.

596 **7 Conclusions**

597 In this study it is shown that the dual node approach should be conceptualized and implemented  
598 as a one-sided finite differences approximation of the vertical hydraulic gradient at the land  
599 surface. This provides an important new insight into the coupling length. Namely, if the dual node  
600 approach is properly implemented then the coupling length is related to the vertical grid resolution.  
601 Thus, the coupling length does not represent an additional non-physical model parameter and  
602 therefore the dual node approach is not automatically a less physically based approach in  
603 comparison to the common node approach. Actually, this study shows if the vertical discretization  
604 is not sufficiently fine then the head continuity at the surface-subsurface interface is formulated  
605 more correctly in the consistent dual node scheme. This difference in formulation has  
606 consequences for how both approaches compare in terms of accuracy and efficiency.

607 Numerical experiment indicate that the consistent dual node approach is equally accurate  
608 or more accurate than the common node approach. It has been shown that in comparison to the  
609 common node approach the consistent dual node approach is less sensitive to the vertical  
610 discretization when simulating excess infiltration. However, the practical advantage of the  
611 consistent dual node approach in terms of accuracy is limited. Namely, if the vertical discretization  
612 is refined, both approaches will converge to more accurate and eventually similar results when  
613 simulating excess infiltration. When simulating excess saturation both approaches yield similar  
614 results even if the vertical discretization is relatively coarse.

615 Nonetheless, even though the advantage of the consistent dual node approach in terms of  
616 accuracy is limited, the fact that the consistent dual node approach is equally or more accurate than  
617 the common node approach is a significant finding. Namely, this finding is different from the  
618 commonly held view that a dual node approach is most accurate if it mimics the common node

619 approach. Moreover, it also illustrates clearly that the consistent dual node approach is not similar  
620 to a common node approach.

621 Numerical experiment indicate that the consistent dual node approach can be more efficient  
622 than the common node approach while being equally or more accurate than the common node  
623 approach. It has been shown that this difference in efficiency is related to abrupt changes in the  
624 evolution of pressure heads around the moment that ponding is initiated.

625 Based on the findings in this study the models of An and Yu [*An and Yu, 2014*] and Kumar  
626 et al. [*Kumar et al., 2009*] are expected to have some advantages with respect to models that are  
627 based on the common node approach. This is because these models are based on a consistent dual  
628 node approach. Moreover, given a model that uses an alternative dual node approach, it is relatively  
629 straightforward to implement the numerically more correct consistent dual node approach.

630

### 631 **Acknowledgements**

632 This research was funded by the Carl. S. Swisher Foundation.

633

### 634 **References**

635 An, H., and S. Yu (2014), Finite volume integrated surface- subsurface flow modeling on  
636 nonorthogonal grids, *Water Resources Research*, 50(3), 2312-2328.

637 Blazek, J. (2005), *Computational fluid dynamics: Principles and applications* *Computational fluid*  
638 *dynamics: Principles and applications*, Elsevier.

639 Camporese, M., C. Paniconi, M. Putti, and S. Orlandini (2010), Surface-subsurface flow modeling  
640 with path-based runoff routing, boundary condition-based coupling, and assimilation of  
641 multisource observation data, *Water Resources Research*, 46.

642 De Rooij, R., W. Graham, and R. Maxwell (2012), A particle-tracking scheme for simulating  
643 pathlines in coupled surface-subsurface flows, *Advances in Water Resources*.

644 de Rooij, R., P. Perrochet, and W. Graham (2013), From rainfall to spring discharge: Coupling  
645 conduit flow, subsurface matrix flow and surface flow in karst systems using a discrete-continuum  
646 model, *Advances in Water Resources*, 61, 29-41.

647 Delfs, J. O., C. H. Park, and O. Kolditz (2009), A sensitivity analysis of Hortonian flow, *Advances*  
648 *in Water Resources*, 32(9), 1386-1395.

649 Diersch, H. J. G., and P. Perrochet (1999), On the primary variable switching technique for  
650 simulating unsaturated-saturated flows, *Advances in Water Resources*, 23(3), 271-301.

651 Ebel, B. A., B. B. Mirus, C. S. Heppner, J. E. VanderKwaak, and K. Loague (2009), First-order  
652 exchange coefficient coupling for simulating surface water-groundwater interactions: parameter  
653 sensitivity and consistency with a physics-based approach, *Hydrological Processes*, 23(13), 1949-  
654 1959.

655 Gaukroger, A. M., and A. D. Werner (2011), On the Panday and Huyakorn surface-subsurface  
656 hydrology test case: analysis of internal flow dynamics, *Hydrological Processes*, 25(13), 2085-  
657 2093.

658 Hillel, D. (1982), *Introduction to soil physics*, Academic press New York.

659 Kolditz, O., and H. Shao (2010), OpenGeoSys, Developer-Benchmark-Book, OGS-DBB 5.04,  
660 Helmholtz Centre for Environmental Research (UFZ).

661 Kollet, S. J., and R. M. Maxwell (2006), Integrated surface-groundwater flow modeling: A free-  
662 surface overland flow boundary condition in a parallel groundwater flow model, *Advances in*  
663 *Water Resources*, 29(7), 945-958.

664 Kumar, M., C. J. Duffy, and K. M. Salvage (2009), A Second-Order Accurate, Finite Volume-  
665 Based, Integrated Hydrologic Modeling (FIHM) Framework for Simulation of Surface and  
666 Subsurface Flow, *Vadose Zone Journal*, 8(4), 873-890.

667 Liggett, J. E., A. D. Werner, and C. T. Simmons (2012), Influence of the first-order exchange  
668 coefficient on simulation of coupled surface-subsurface flow, *Journal of Hydrology*, 414, 503-515.

669 Liggett, J. E., M. J. Knowling, A. D. Werner, and C. T. Simmons (2013), On the implementation  
670 of the surface conductance approach using a block-centred surface-subsurface hydrology model,  
671 *Journal of Hydrology*, 496, 1-8.

672 Morita, M., and B. C. Yen (2002), Modeling of conjunctive two-dimensional surface-three-  
673 dimensional subsurface flows, *Journal of Hydraulic Engineering-Asce*, 128(2), 184-200.

674 Moukalled, F., L. Mangani, and M. Darwish (2016), *The Finite Volume Method in Computational*  
675 *Fluid Dynamics*, Springer.

676 Osei-Kuffuor, D., R. M. Maxwell, and C. S. Woodward (2014), Improved numerical solvers for  
677 implicit coupling of subsurface and overland flow, *Advances in Water Resources*, 74, 185-195.

678 Pan, L., and P. J. Wierenga (1995), A transferred pressure head based approach to solve Richards  
679 equation for variably saturated soils, *Water Resources Research*, 31(4), 925-931.

680 Panday, S., and P. S. Huyakorn (2004), A fully coupled physically-based spatially-distributed  
681 model for evaluating surface/subsurface flow, *Advances in Water Resources*, 27(4), 361-382.

682 Ross, P. J. (1990), Efficient numerical methods for infiltration using Richards equation, *Water*  
683 *Resources Research*, 26(2), 279-290.

684 Sulis, M., S. B. Meyerhoff, C. Paniconi, R. M. Maxwell, M. Putti, and S. J. Kollet (2010), A  
685 comparison of two physics-based numerical models for simulating surface water-groundwater  
686 interactions, *Advances in Water Resources*, 33(4), 456-467.

687 Therrien, R., R. G. McLaren, E. A. Sudicky, and S. M. Panday (2010), HydroGeoSphere-a three-  
688 dimensional numerical model describing fully-integrated subsurface and surface flow and solute  
689 transport (draft), Groundwater Simulations Group, University of Waterloo.

690 VanderKwaak, J. E. (1999), Numerical simulation of flow and chemical transport in integrated  
691 surface-subsurface hydrologic systems, University of Waterloo.

692 Yeh, G.-T., D.-S. Shih, and J.-R. C. Cheng (2011), An integrated media, integrated processes  
693 watershed model, *Computers & Fluids*, 45(1), 2-13.

694 Zienkiewicz, O., R. Taylor, and J. Zhu (2005), The finite element method: its basis and  
695 fundamentals. 2005, edited, Butterworth-Heinemann.

696

697

698

699

700

701

abbreviation	meaning
cc	cell-centered
vc	vertex-centered
dn	dual node
cn	common node

702

703 Table 1: Abbreviations as used in the figures.

704

705

706

707

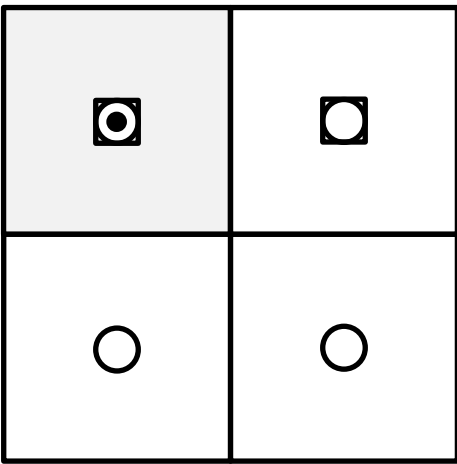
708

709

710

711

a)



712

713

714

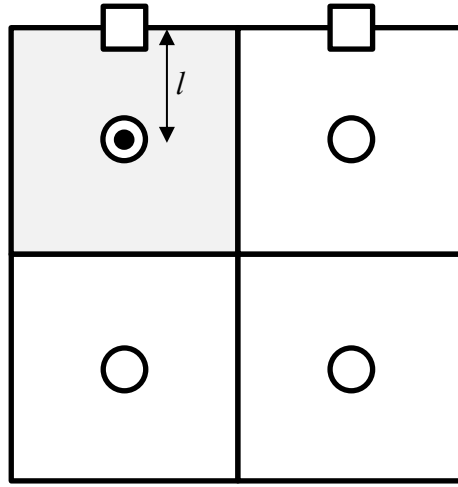
715

716

717

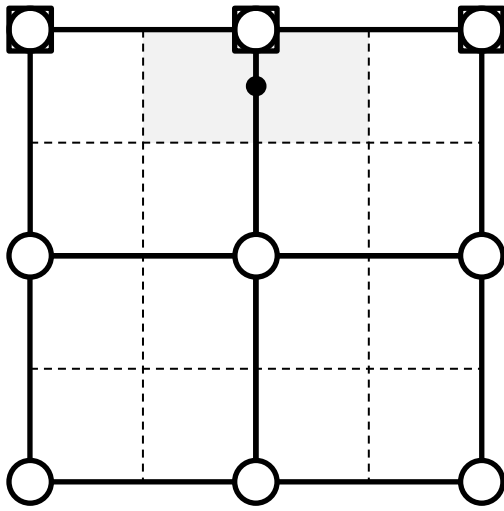
718

b)



719

c)



720

721

722

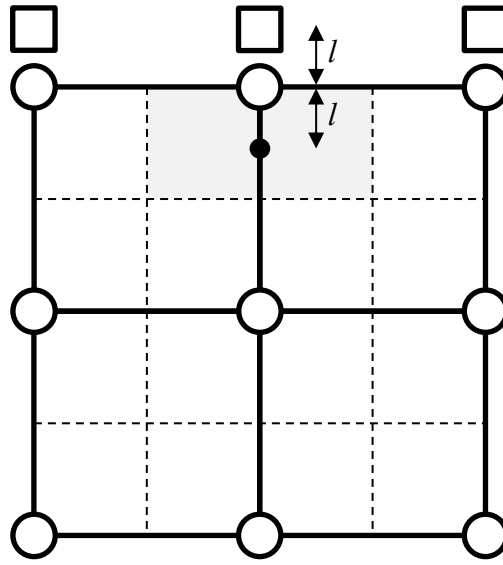
723

724

725

726

d)



727

728

729

730



731 Figure 1: a) Common nodes in cell-centered schemes. b) Dual nodes in cell-centered-centered  
732 schemes. c) Common nodes and co-located dual nodes in vertex-centered schemes. d) Dual nodes  
733 in vertex-centered schemes (not co-located). The white squares and white circles represent surface  
734 and subsurface nodes, respectively. The solid and dashed lines represent the primary mesh and the  
735 dual mesh, respectively. The grey-shaded area is a topmost discrete volume as associated with a  
736 topmost subsurface node. The black dot represents the centroid of this volume. The coupling length  
737  $l$  as depicted in this figure applies to the consistent dual node approach.

738

739

740

741

742

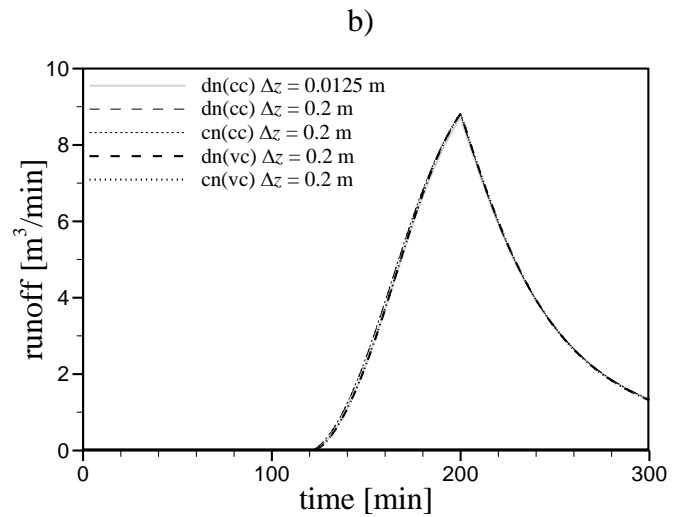
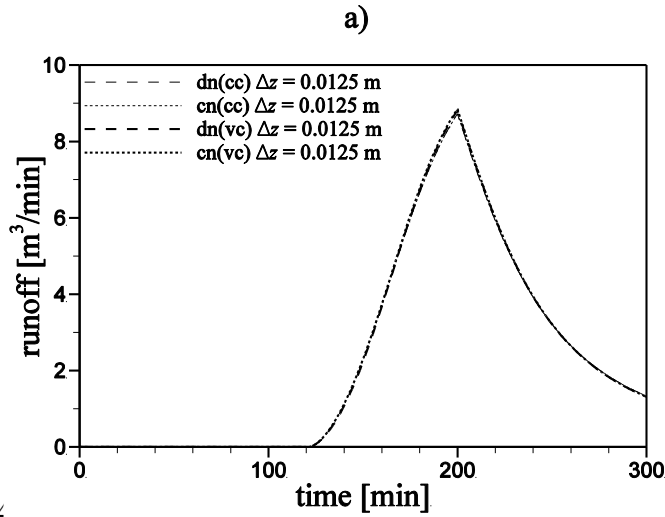
743

744

745

746

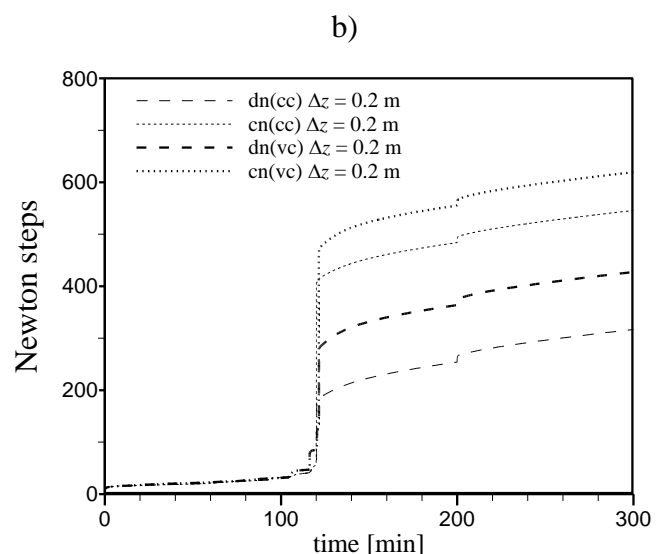
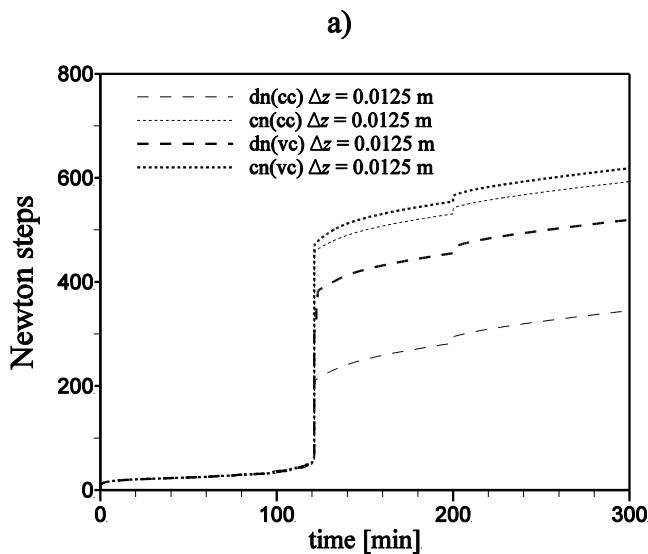
747



748

749 Figure 2: Outflow response for excess saturation on a hillslope (first scenario) using different  
750 vertical discretizations.

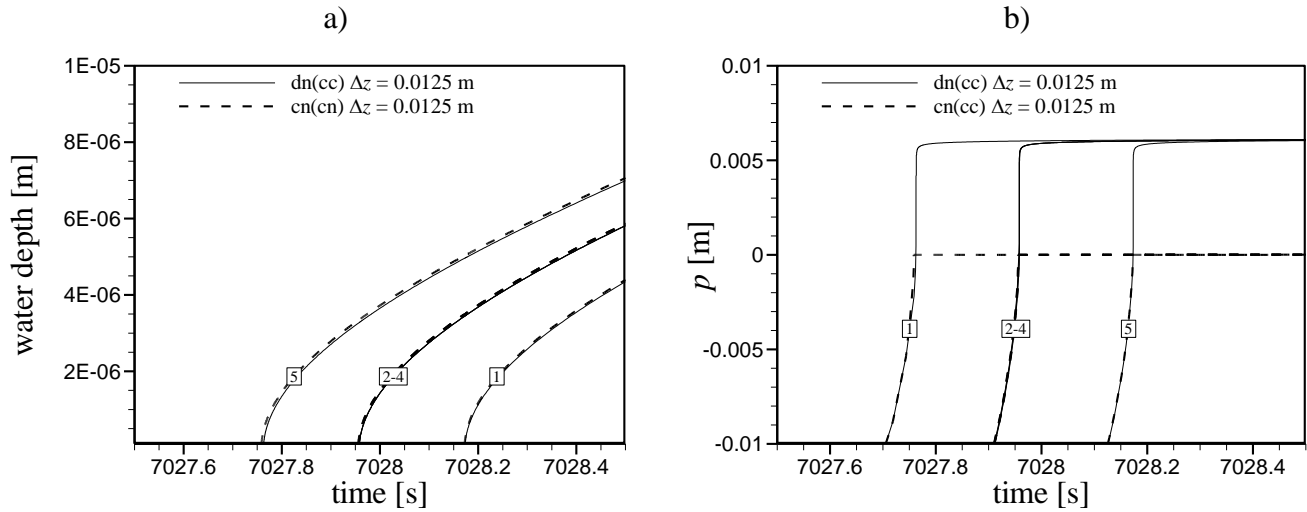
751



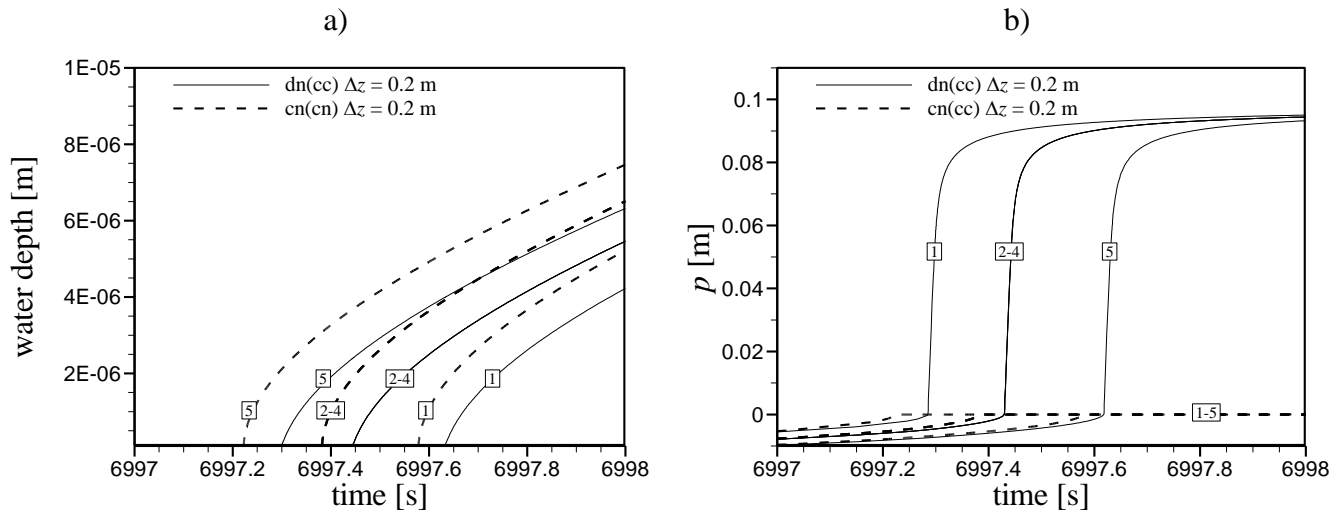
752

753 Figure 3: Number of Newton steps for excess saturation on a hillslope (first scenario) using  
754 different vertical discretizations.

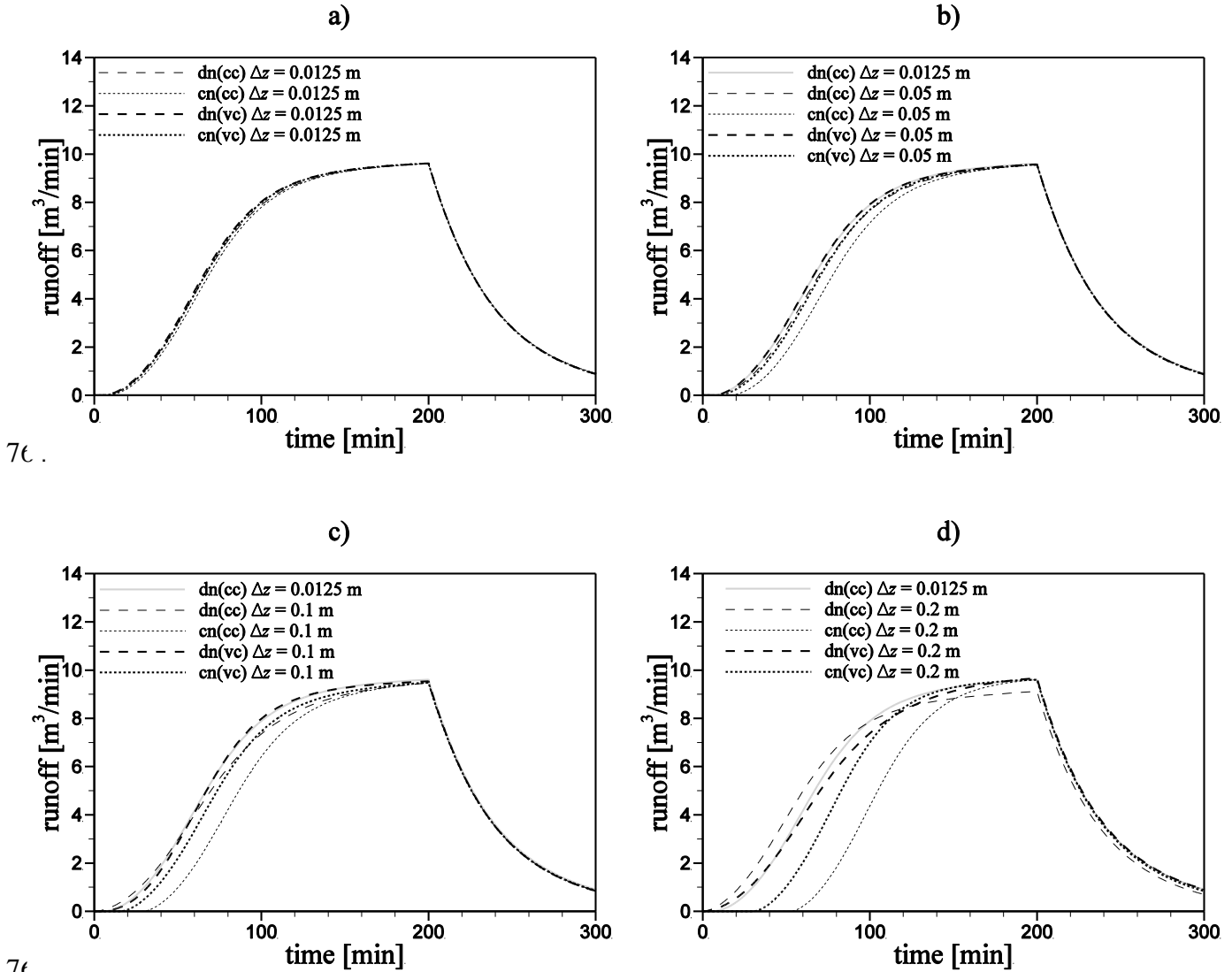
755



757 Figure 4: Simulated values at the common nodes for excess saturation on a hillslope (first scenario)  
 758 with a cell-centered scheme and  $\Delta z = 0.0125$  m. a) Water depths. b) Pressure heads. Nodes are  
 759 numbered 1-5 in the down-slope direction.



761 Figure 5: Simulated values for excess saturation on a hillslope (first scenario) with a cell-centered  
 762 scheme and  $\Delta z = 0.2$  m. a) Water depths at the surface nodes. b) Pressure heads at the topmost  
 763 subsurface nodes. Nodes are numbered 1-5 in the down-slope direction.



766 Figure 6: Outflow response for excess infiltration on a hillslope (second scenario) using different  
 767 vertical discretizations.

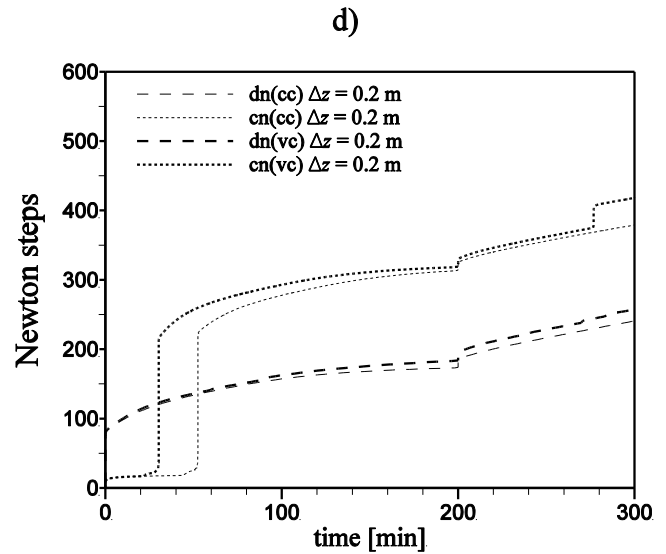
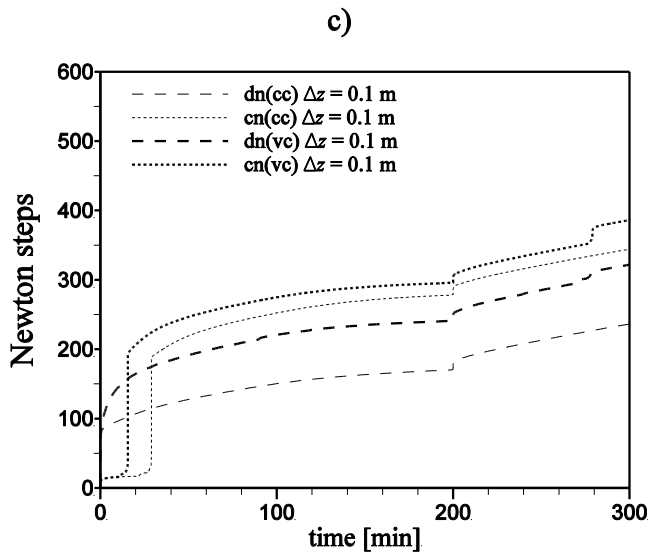
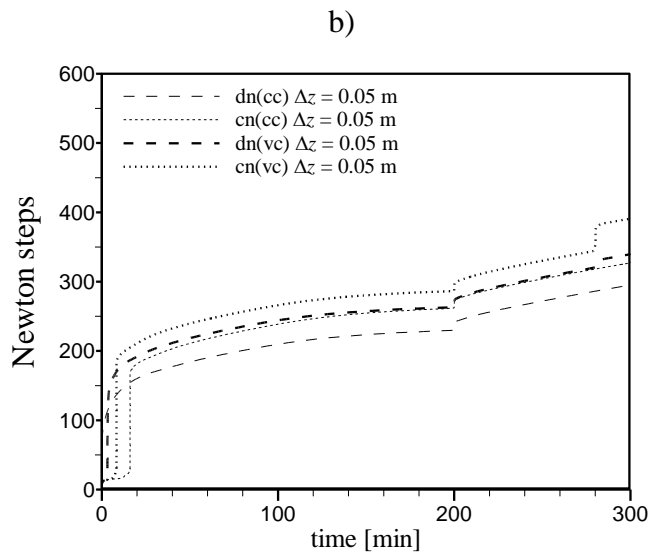
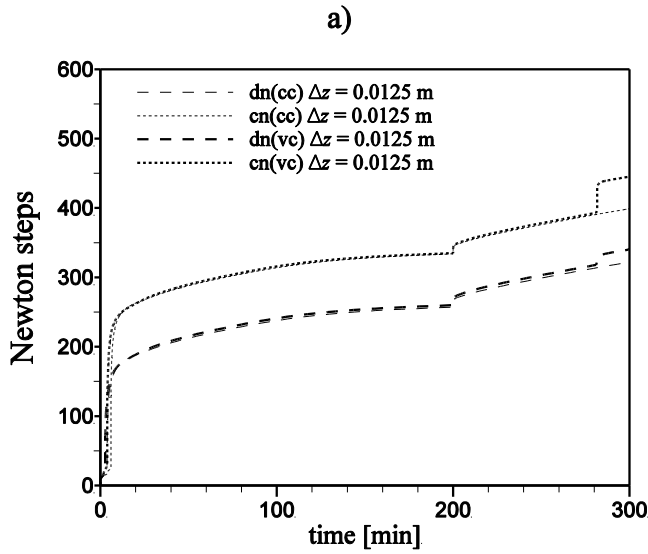
768

769

770

771

772



775

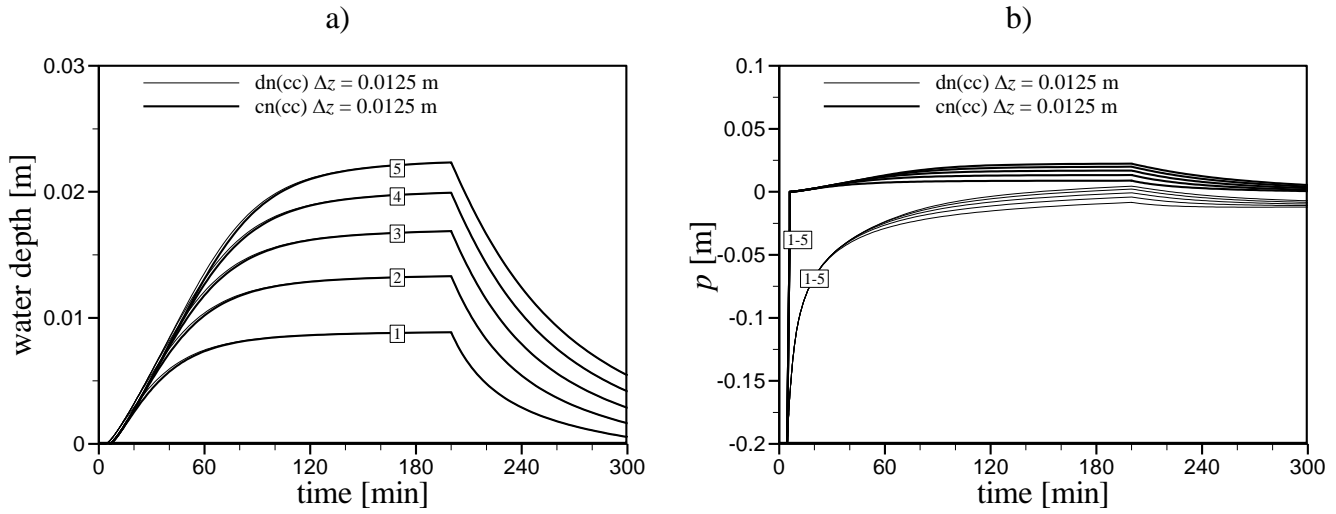
776 Figure 7: The total number of Newton steps for excess infiltration (second scenario) on a hillslope  
 777 using different vertical discretizations.

778

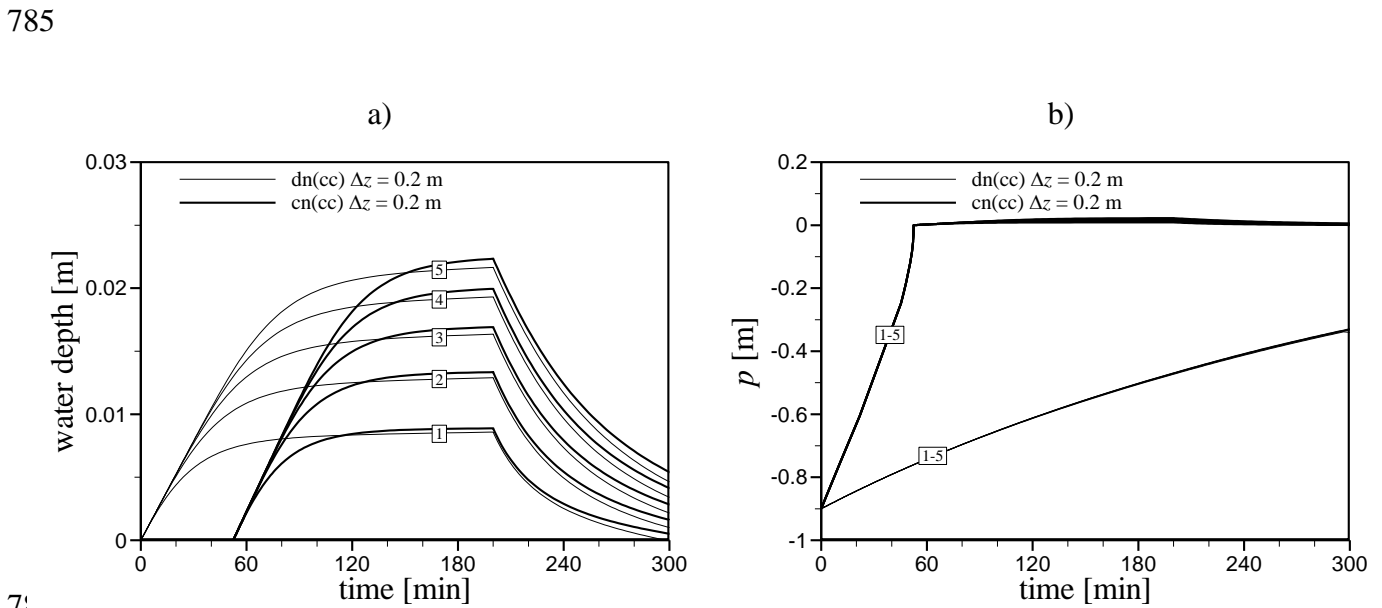
779

780

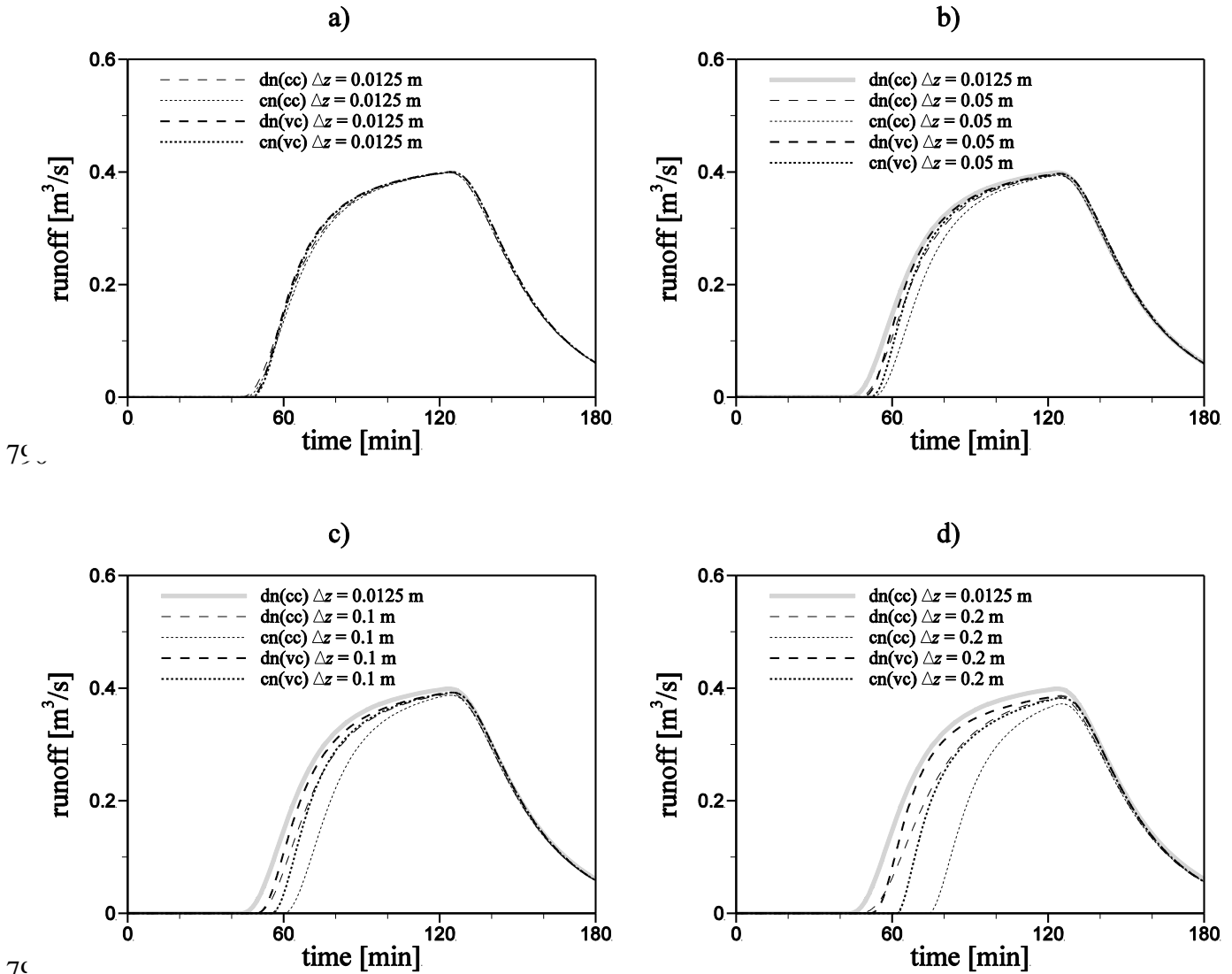
781



781  
 782 Figure 8: Simulated values at the common nodes for excess infiltration on a hillslope (second  
 783 scenario) with a cell-centered scheme and  $\Delta z = 0.0125$  m. a) Water depths. b) Pressure heads.  
 784 Nodes are numbered 1-5 in the down-slope direction.



785  
 786  
 787 Figure 9: Simulated values for excess infiltration on a hillslope with a cell-centered scheme  
 788 (second scenario) and  $\Delta z = 0.2$  m. a) Water depths at the surface nodes. b) Pressure heads at the  
 789 topmost subsurface nodes. Nodes are numbered 1-5 in the down-slope direction.



792 Figure 10: Outflow response for flooding an unsaturated hillslope using different vertical  
 793 discretizations.

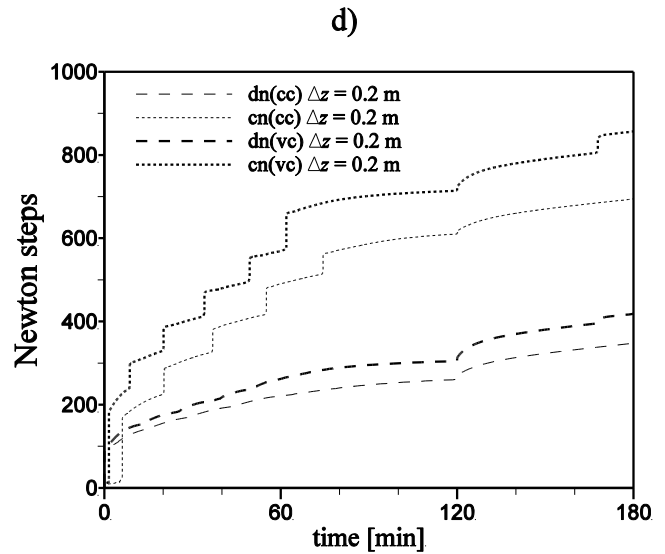
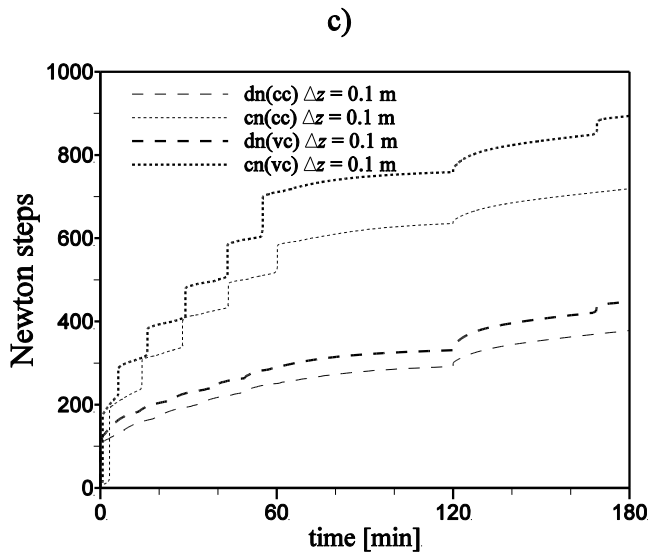
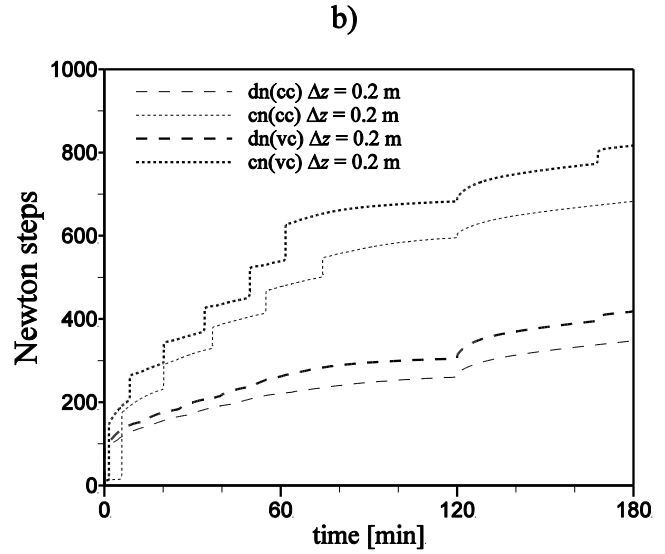
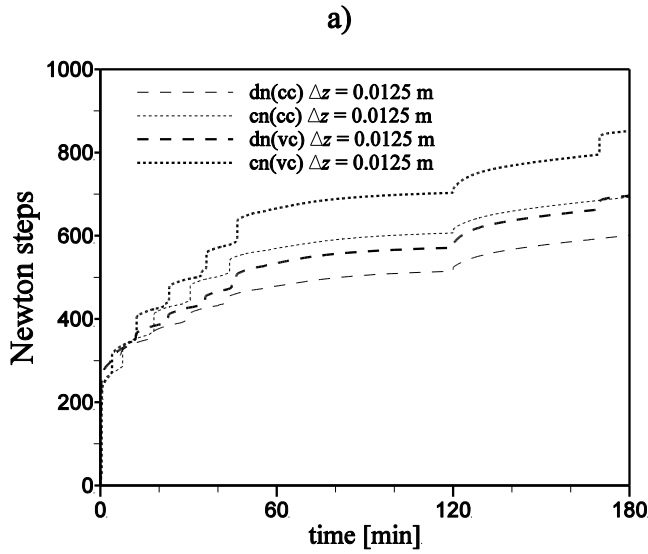
794

795

796

797

798



79

80

801 Figure 11: Number of Newton steps for flooding an unsaturated hillslope using different vertical  
 802 discretizations.

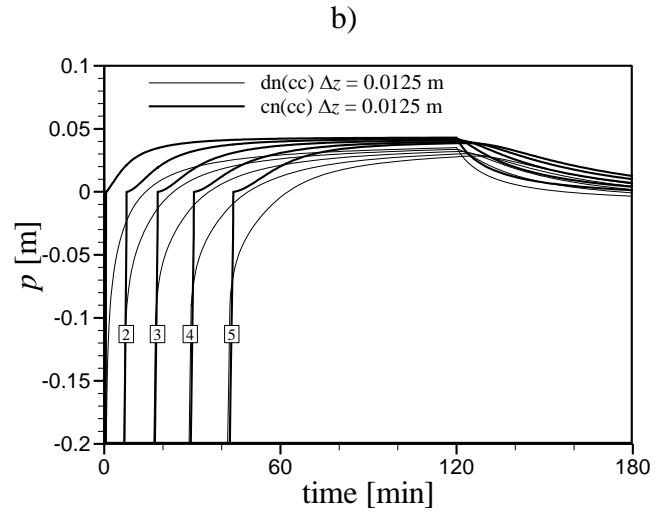
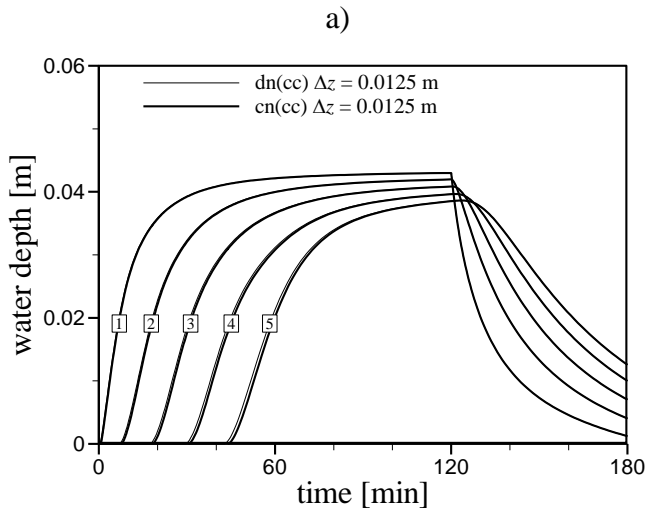
803

804

805

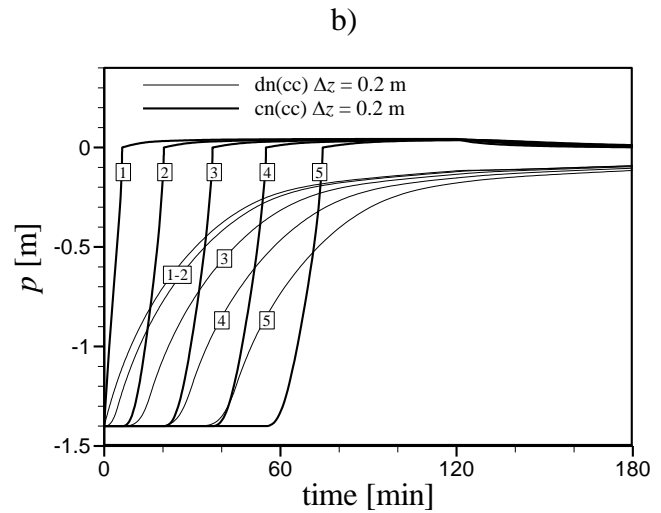
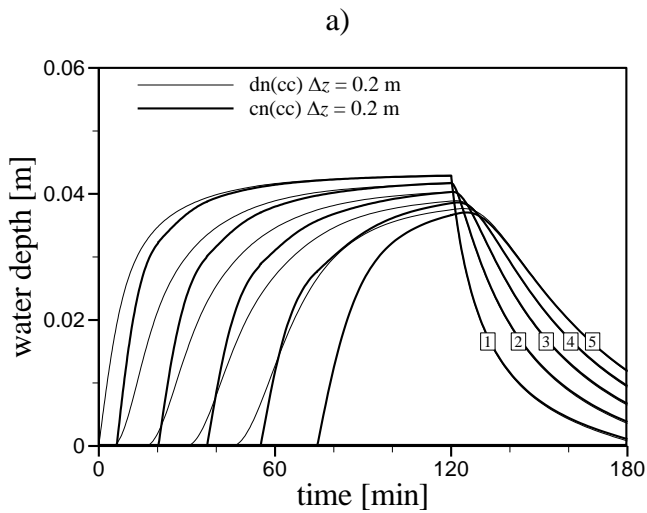
806





80

808 Figure 12: Simulated values for excess infiltration (third scenario) on a hillslope with a cell-  
 809 centered scheme and  $\Delta z = 0.0125$  m. a) Water depths at the surface nodes. b) Pressure heads at the  
 810 topmost subsurface nodes. Nodes are numbered 1-5 in the down-slope direction).



8

812 Figure 13: Simulated values for excess infiltration (third scenario) on a hillslope with a cell-  
 813 centered scheme and  $\Delta z = 0.2$  m. a) Water depths at the surface nodes. b) Pressure heads at the  
 814 topmost subsurface nodes. Nodes are numbered 1-5 in the down-slope direction).

815